

The Effect of Ti on Physical Properties of Fe₂O₃ Thin Films for Gas Sensor Applications

Sami Salman Chiad^{1*} and Tahseen H. Mubarak²

¹Department of Physics, College of Education, AlMustansiriyah University, Baghdad, Iraq.

²Department of Physics, College of Science, University of Diyala, Diyala, Iraq.

Received 19 June 2019, Revised 7 November 2019, Accepted 17 January 2020

ABSTRACT

Hematite (Fe₂O₃) and titanium (1 wt% and 3 wt%) doped Fe₂O₃ were prepared onto glass and p-type silicon wafer using the pulsed laser deposition technique. X-ray diffraction analysis indicates that samples of pure and Ti-doped were polycrystalline with a crystal orientation along (113) plane. The average grain size increases with the increasing titanium content. Surface morphology was studied through a Scanning Electron Microscope (SEM) and Atomic Force Microscopy (AFM), which reveal that grains are columnar in shape. UV-visible transmission spectroscopy reveals that the deposited films are transparent within a visible range. The value of the optical bandgap exhibits a decrease from 1.93 eV to 1.48 eV as titanium concentration increases. Gas sensitivity measurements at 30°C. showed a decrease in sensitivity with the increase of doping and gas concentration.

Keywords: Fe₂O₃, Ti, SEM, AFM and Gas Sensitivity.

1. INTRODUCTION

With the development of science, especially in the field of nanotechnology, metal oxide has become one of the significant materials in nanotechnology applications [1]. Metal oxide can be n-type or p-type semiconductor [2]. Hematite is one of the common metal oxide also known as iron oxides with chemical composition of α -Fe₂O₃. Hematite has a great importance for various applications and it can be used as a catalyst [3], photocatalysis [4], gas sensor [5], biomedicine [6], data storage [7], environmental remediation [8], and electrical magnetic resonance imaging [9]. Hematite has stoichiometry with poor conductivity, but the addition of metal impurities shall improve its stoichiometry, electrical and structural properties [10]. Hence, there is a widespread interest in the use of hematite in gas sensor applications, which have common characteristics between the p-type and n-type that make them suitable for measurement of oxidized and reduced gases. Hematite has an energy gap of 1.5 eV - 2.0 eV [11]. The phase of hematite is characterized by an octahedral unit cell type [12].

Several physical and chemical properties of hematite are studied in this research. Measurements related to the sensitivity of hematite was done by Cheng et al. [13] as they prepared porous Fe₂O₃ doped with palladium (Pd) nanotubes for ethanol gas sensing. Meanwhile, Wu et al. [14] made a sensor for hydrogen sulphide (H₂S) gas using α -Fe₂O₃ nano-ellipsoids and Yan et al. [15] prepared α -Fe₂O₃ nanorhombs sensor for ethanol gas. Pulsed Laser Deposition (PLD) method has certain advantages such as high precision, high purity, and high sensitivity to gases [16]. Moreover, some methods available for the deposition of α -Fe₂O₃ hematite includes RF and DC sputtering [17], thermal evaporation [18], and reactive beam sputtering [19]. The current study focuses the

*Corresponding Author: dr.sami@uomustansiriyah.edu.iq

attention on the preparation of Ti-doped Fe_2O_3 films by pulsed laser deposition. In addition, their physical properties and sensing characterization are studied for the first time.

2. MATERIAL AND METHODS

Hematite (Fe_2O_3) and Ti (1 wt% and 3 wt%) doped Fe_2O_3 are prepared onto glass and p-type silicon wafer using a pulsed laser deposition technique. The deposition system contains Q-switched Nd-YAG laser operated at 532 nm with a pulse duration of 8 ms and an energy density of 0.4 J/cm^2 . The main reason for choosing this technique is its ability to introduce the possibility of synthesized metastable phases, which are hopeless under thermal conditions. The thickness of the deposited film is evaluated through the gravimetric method. The films thickness is in the range of 350 nm.

X-ray diffraction (XRD) patterns were used to obtain the structure of the deposited thin films through the use of Philips PW 1840 X-ray diffractometer with a wavelength of 1.541 \AA from $\text{CuK}\alpha$. Atomic Force Microscope (AFM) from Angstrom company (AA3000) Scanning Probe Microscope was used to determine surface topography. The morphology of the deposited thin film was measured using Scanning Electron Microscope (SEM). Hall coefficient (RH), charge carriers and mobility of the deposited thin films were estimated using a device (HMS-3000). Transmittance and absorbance spectra were recorded by a double beam spectrophotometer (Shimadzu UV probe 1640 Japan) in the wavelength range of (300 - 900) nm. The gas sensing measurement testing system is shown in Figure (1).

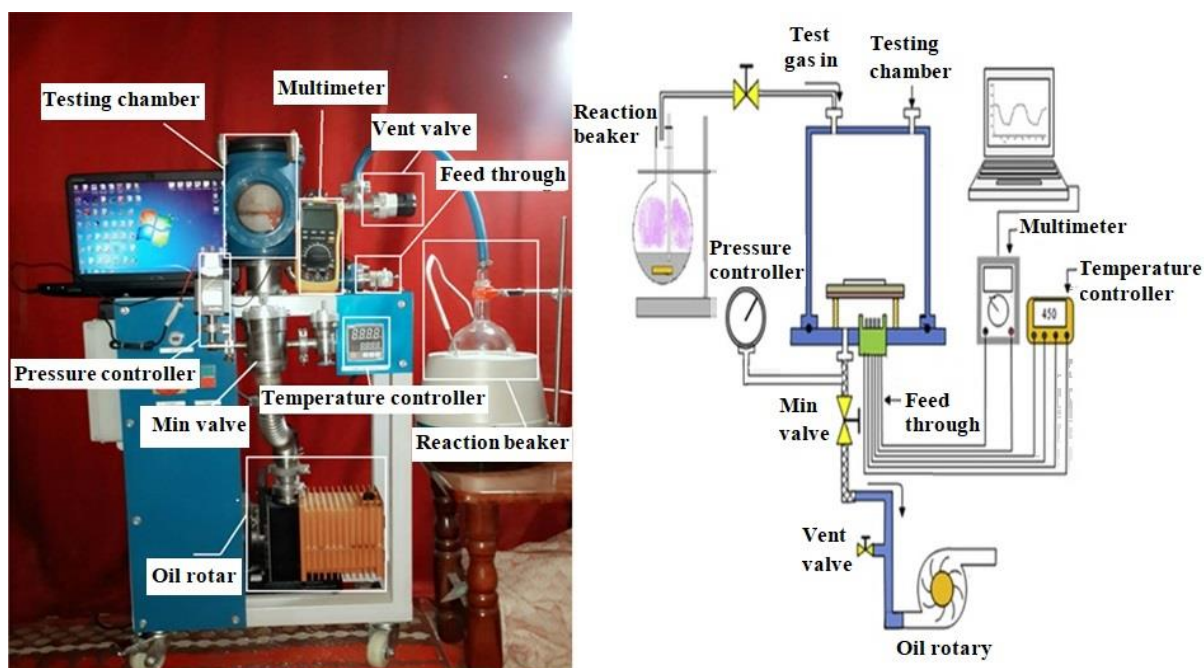


Figure 1. Gas Sensor Testing System.

3. RESULTS AND DISCUSSION

Figure (2-a) represents the x-ray diffraction patterns of $\text{Fe}_2\text{O}_3:\text{Ti}$ deposited by a pulsed laser deposition technique. From the figure, it is noticed that all the recorded membranes are polycrystallized with an ideal reflection at (113) plane at the angle of $2\theta=31.26^\circ$. The intensity of this reflection increases with the increase of Ti doping. The crystallite size increased from 16.65 nm to 23.09 nm with the increase of Ti content, where Figure (2-b) shows the zoom in for the ideal

reflection (113) where full width at half maximum (FWHM) decrease is associated with the increase of the crystallite size obtained via Scherrer equation (1) [20].

$$D = \frac{0.9\lambda}{\beta \cos\theta} \quad (1)$$

Where β (FWHM) and λ is the X-ray wavelength (1.54056Å).

Figure. (2- c, d and e) represent SEM images of the pure and doped films with 1 wt% and 3 wt%, respectively. A secondary reflection at (201), (207) and (300) at the angles of 35.09°, 39.32°, 53.62° respectively are noticed, which were in good agreement with ICDD card no. 40-1136. Figure (3) represents the values of FWHM, microstrain and dislocation density, calculated from the x-ray diffraction pattern, where the microstrain and dislocation density values decreased with the increase of crystallite size. Table (1) reflects the extracted values from x-ray diffraction patterns.

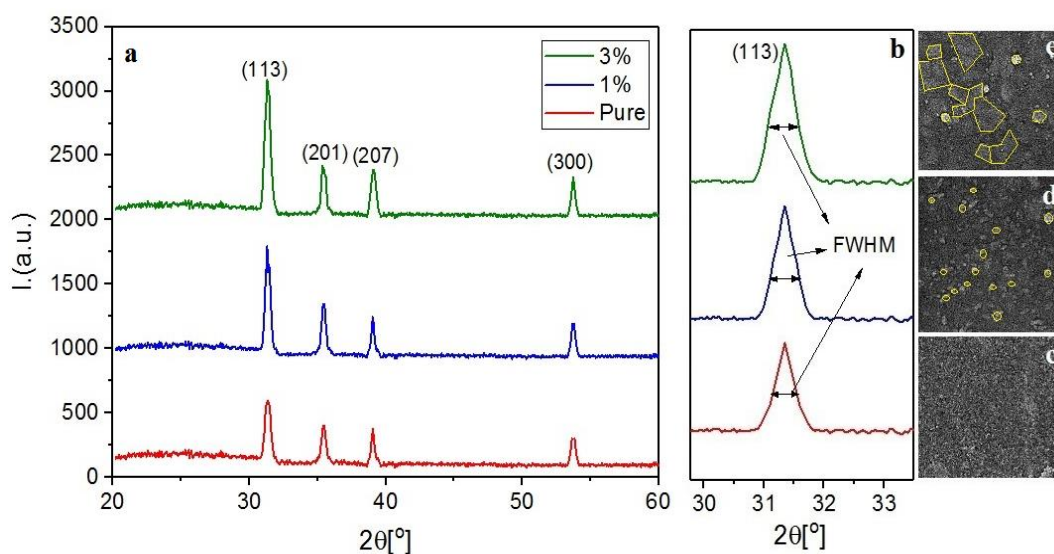


Figure 2. (a) XRD pattern of pure Fe₂O₃ and Ti-doped, (b) the screenshot of the zoom in of ideal reflection, (c), (d) and (e) SEM images of the pure and doped of (blue) 1 wt % and (green) 3 wt % Ti.

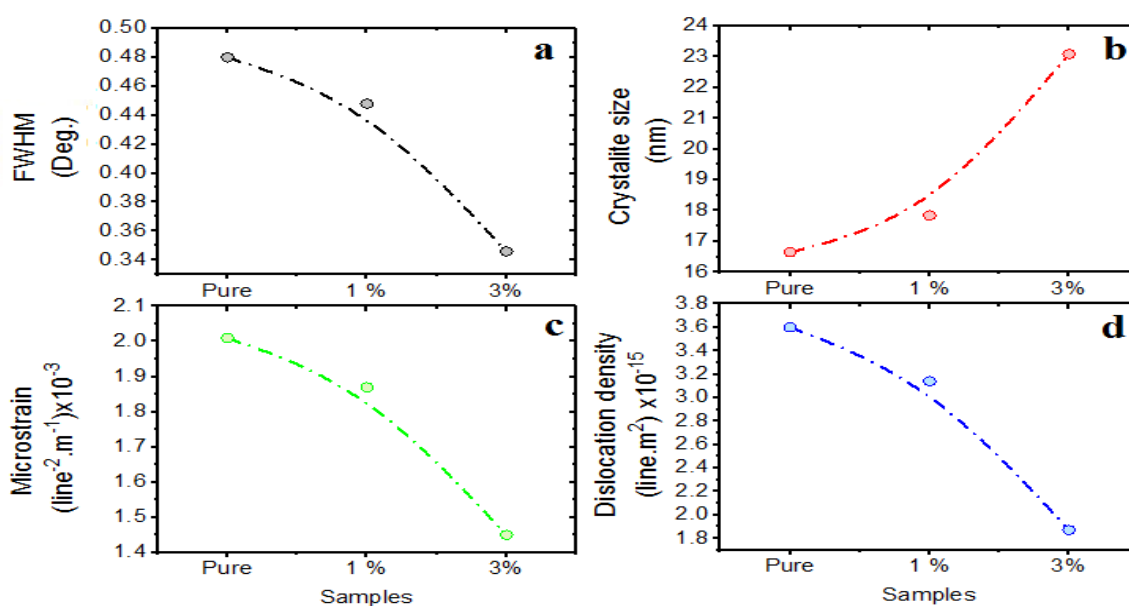


Figure 3. (a) FWHM, (b) Crystallite size, (c) Microstrain and (d) Dislocation density of the deposited films.

Table 1 X-ray diffraction parameters

Samples Ti (%)	(hkl) Plane	2 θ ($^{\circ}$)	FWHM ($^{\circ}$)	(D) (nm)	Microstrain (Line $^{-2}$.m $^{-1}$) $\times 10^{-2}$	Dislocation Density (δ) (Line. m $^{-2}$) $\times 10^{15}$	Calculated	
							A (\AA)	B (\AA)
0	(113)	31.26	0.48	16.651	2.013	3.606	5.140	35.865
1	(113)	31.18	0.448	17.840	1.879	3.142	5.140	35.395
3	(113)	31.22	0.346	23.099	1.451	1.874	5.140	35.987

Figure (4- a, b and c) represents the SEM images of the undoped Fe₂O₃ film, which shows that the thickness of the deposited film is 87.35 nm. Figure (4- a2 and a3) indicate that the surface is heterogeneous and contain areas representing the developing seeds to form crystals. There are atoms of Fe₂O₃ in the form of circular clusters and the particle size is about 12-18 nm. Figure (4-a4) is the EDX, which assures that films are composed only of Fe and O. Figure (4- b1, b2 and b3) represents the SEM images of Fe₂O₃ thin with 1 wt% of Ti content. Figure (4-b1) shows that film thickness increased to 138.97 nm. From figure (5- b and c), the film surface was more frequent and more widespread than the undoped, and the crystallite size increased to a range of 13-20 nm. Figure (4-b4) represents the EDX measurement, which indicates that this sample composed of O, Ti, and Fe. Figure (4- c1, c2 and c3) represents the SEM images of 3% Ti dope Fe₂O₃ film. Figure (6-a) shows that the film thickness increased to 140.36 nm and Figure (4- c2 and c3) show that the film surface is wider than the two previous samples. The crystallite size increased to a range of 15-21 nm and took the form of nanotubes. Figure (4-c4) represents the EDX measurement and represents the existence of Fe, O, Ti in the film composition.

On the other hand, Figure (5-a1) represents the measurement of AFM of undoped Fe₂O₃ sample, where the distribution of atoms as a function of their diameter was included. The average particle size is 50 nm and the average roughness is 2.92 nm. In addition, Figure (5-a1) represents a three-dimensional image and the growth of structures is indicated in the form of columns. Figure (5-b1) represents the AFM images of 1% Ti-doped Fe₂O₃ thin films. The average diameter size is 70 nm and the average roughness is 4.00 nm. Figure (5-b2) represents a three-dimensional image which displays the growth of structures in the form of columns that became higher and more widespread than the undoped sample. Figure (5-c1) represents the measurement of AFM of 3% Ti-doped Fe₂O₃. The distribution of atoms as a function of the diameters is included in the two-dimensional form. The average diameter is 80 nm and the roughness rate is 2.52 nm. The three-dimensional image shown in Figure (5) indicates that columns have become intertwined among them, and the radius of each columns are wider than 1 wt% of titanium.

Figure (6) represents the transmittance as a function of wavelength, which decreases from 88% to 80% with the increase of doping. The decreased might be due to the absorption of impurities since their ionization energy lies near the energy gap of incident photons. Thus, it is consistent with the increase in surface roughness. Figure (7) represents the optical energy gap values of the deposited films, which are observed through the decrease of the values of the energy gap from 1.93 eV to 1.48 eV as the doping ratio increases up to 3 wt%. This might be due to the increase in crystallization and particle size [21].

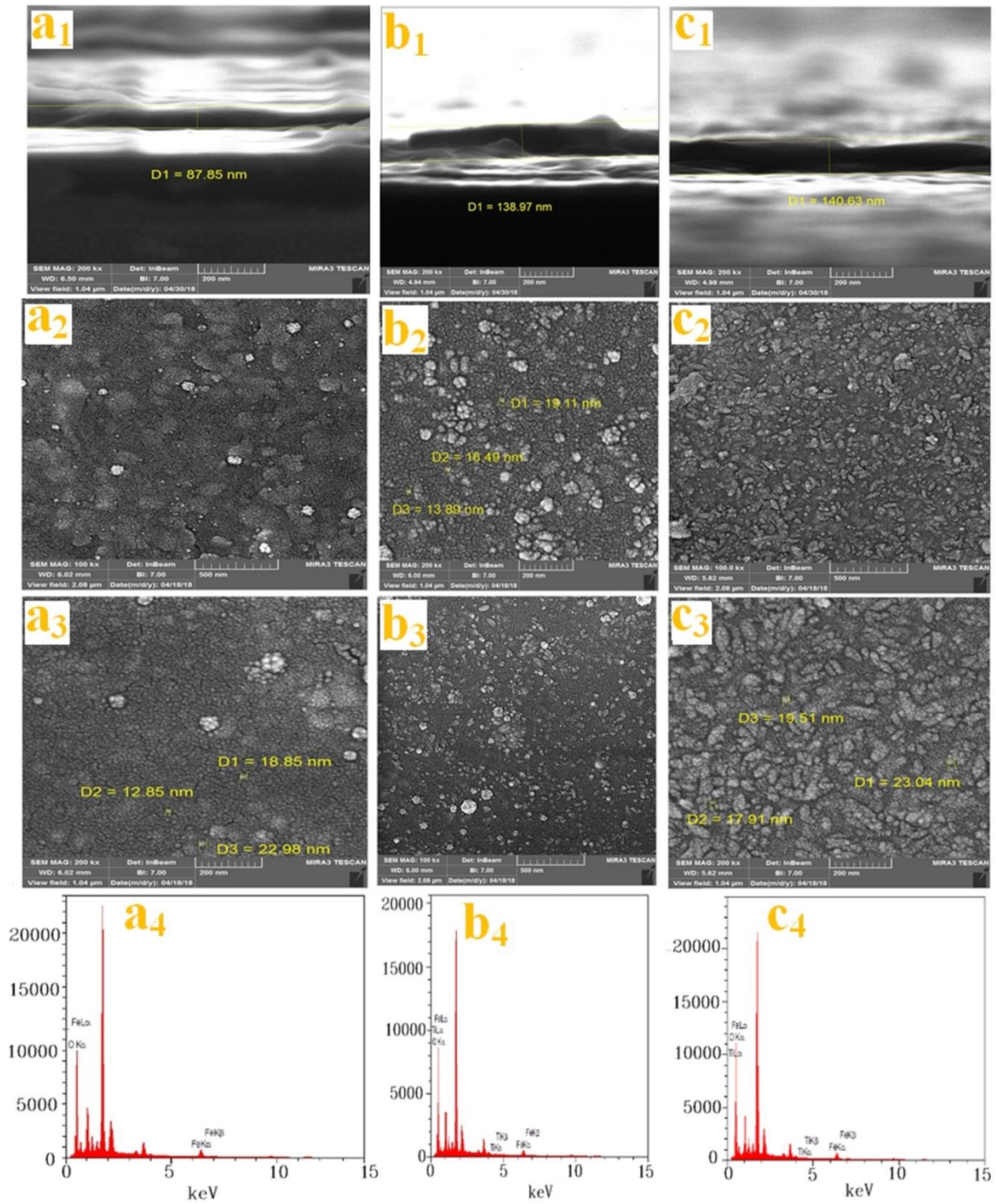


Figure 4. SEM images and EDX of (a) undoped Fe_2O_3 , (b) 1% doped by Ti, and (c) 3% doped by Ti.

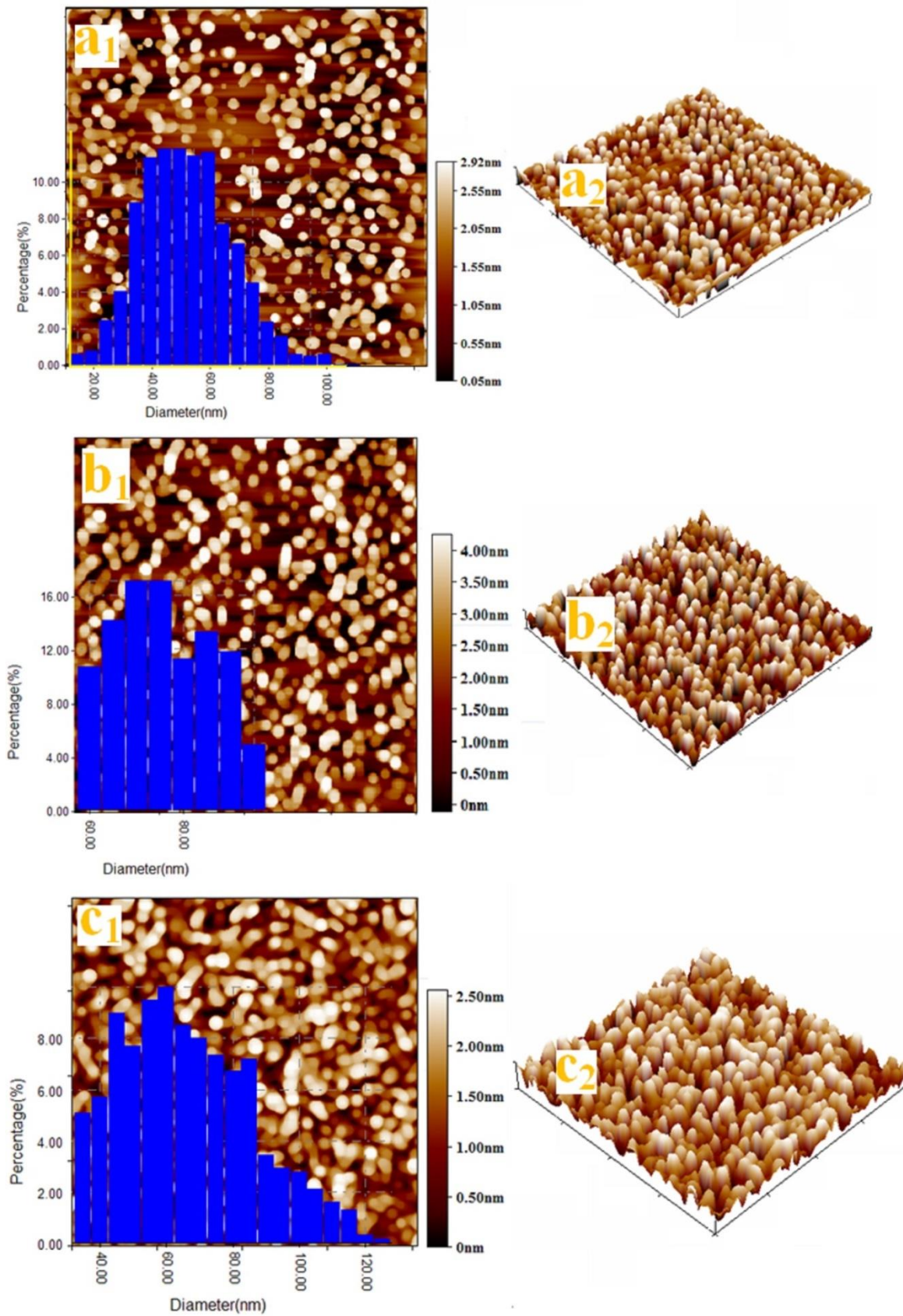


Figure 5. AFM images (a) undoped Fe_2O_3 , (b) 1% doped by Ti, and (c) 3% doped by Ti.

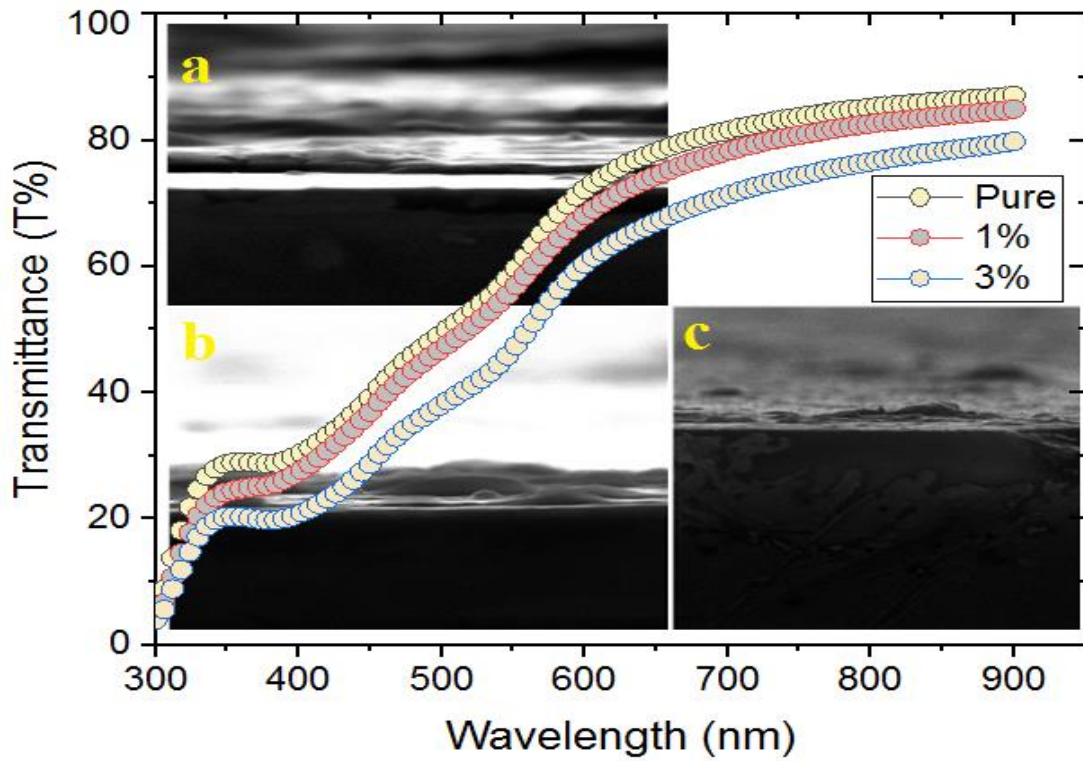


Figure 6. Transmittance as a function of wavelengths of the deposited films.

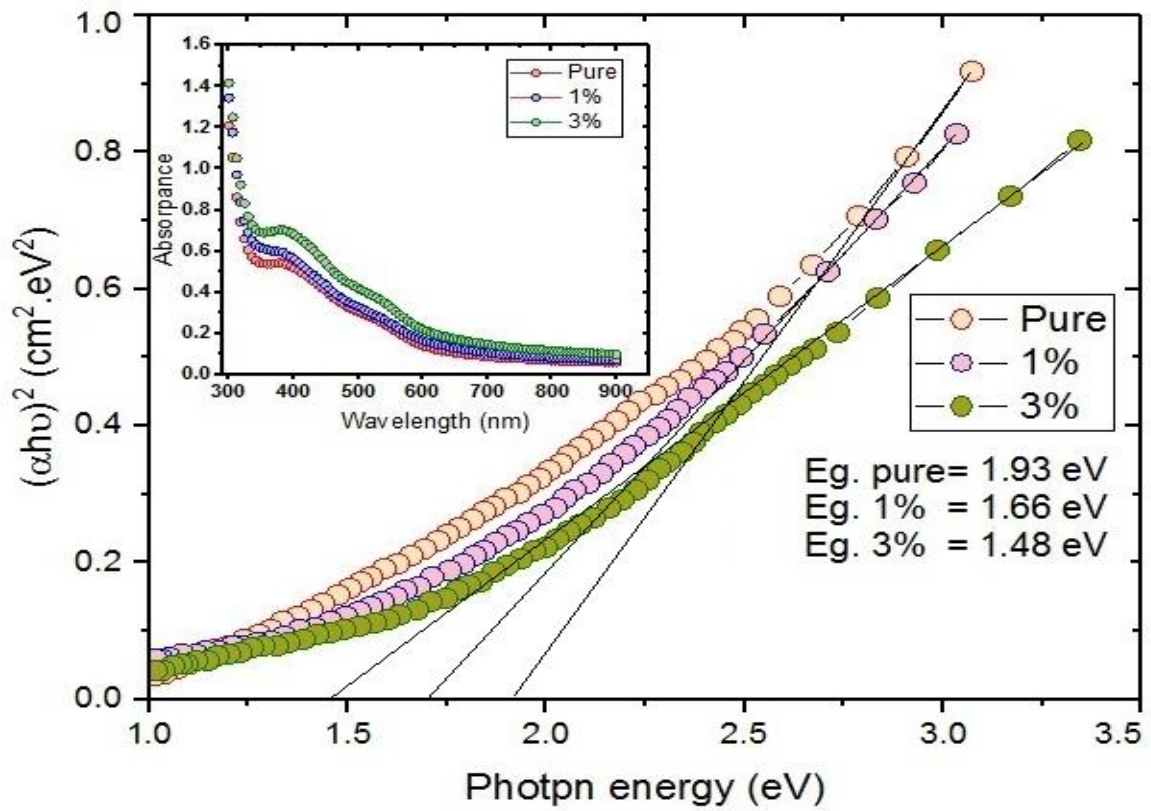


Figure 7. Photon energy as a function to the $(\alpha h\nu)^2$ of the deposited films.

Figure (8) shows the measured PL spectra of pure and Ti-doped Fe_2O_3 films prepared by pulsed laser deposition. A single peak for each sample was observed and shifted towards the higher wavelengths, indicating a change in the energy values of the bands. In other words, the values of the energy gap (see red marker) increased from 634 nm to 640 nm and to 645 nm for the pure, 1 wt% and 3 wt% Ti content, respectively. This could be attributed to the recombination through point defects in the Fe_2O_3 doping by Ti, such as oxygen vacancies, iron vacancies, oxygen interstitials, and titanium interstitial [22]. The PL intensity of all peaks is at 645 nm. This suggests that Fe_2O_3 is a well crystalline structure, while the lower two intensities broadening emission refer to the defects in the film that shifted towards long wavelength indicating nanostructures phenomena, this result agrees with the XRD and SEM results.

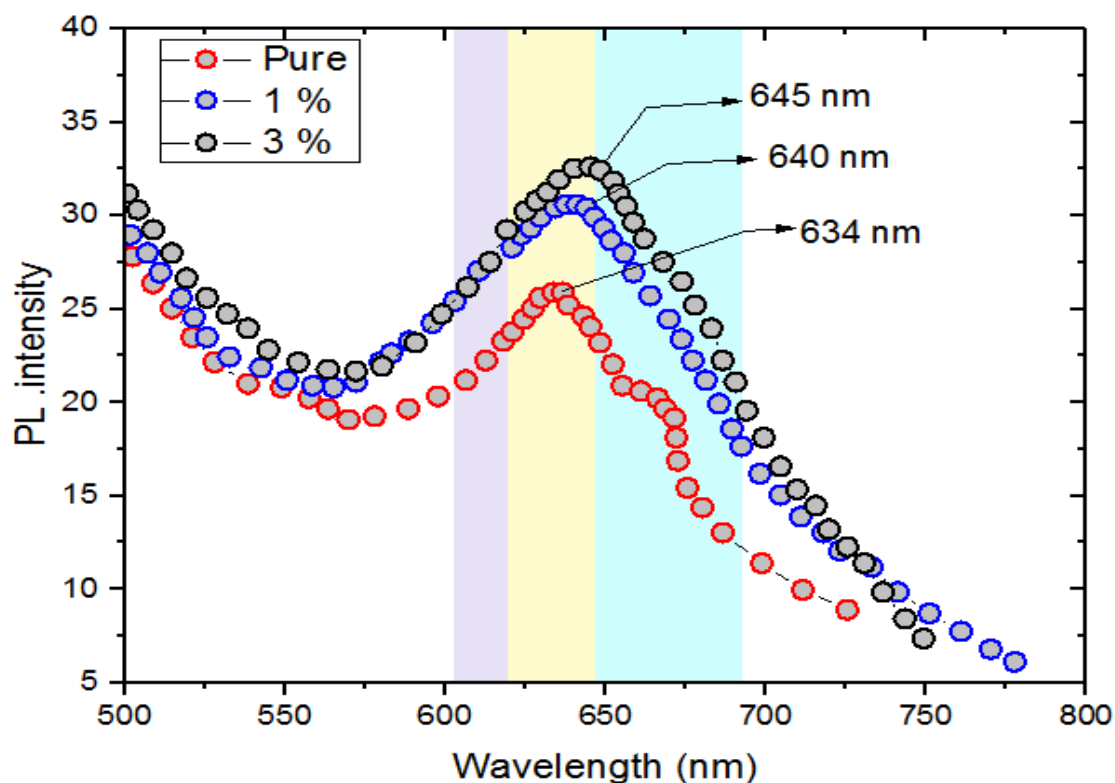


Figure 8. Photoluminescence as a function of wavelength of the Fe_2O_3 films doped by 1wt % and 3wt %Ti.

Four probes Van Der Pauw method was applied to determine the Hall Parameters, Figure (9) represents the electrical measurements, charge carrier concentration, mobility, Hall coefficient, and resistivity. It is noticed that all carrier concentration values are positive (R_H) indicating that the films exhibit the p-type conduction. The results show an obvious decrease in the value of electrical resistivity along with a clear increase in the values of charge carriers, mobility and Hall coefficient. The mobility limit increases with the increasing doping content. The results may be attributed to the average particle size that increases with the increase of the doping concentration as shown by the x-ray diffraction. Therefore, the doping concentration in Fe_2O_3 thin films plays a vital role in determining its electrical properties [23]. Figure (9) shows all the parameters under investigation as a function of concentration.

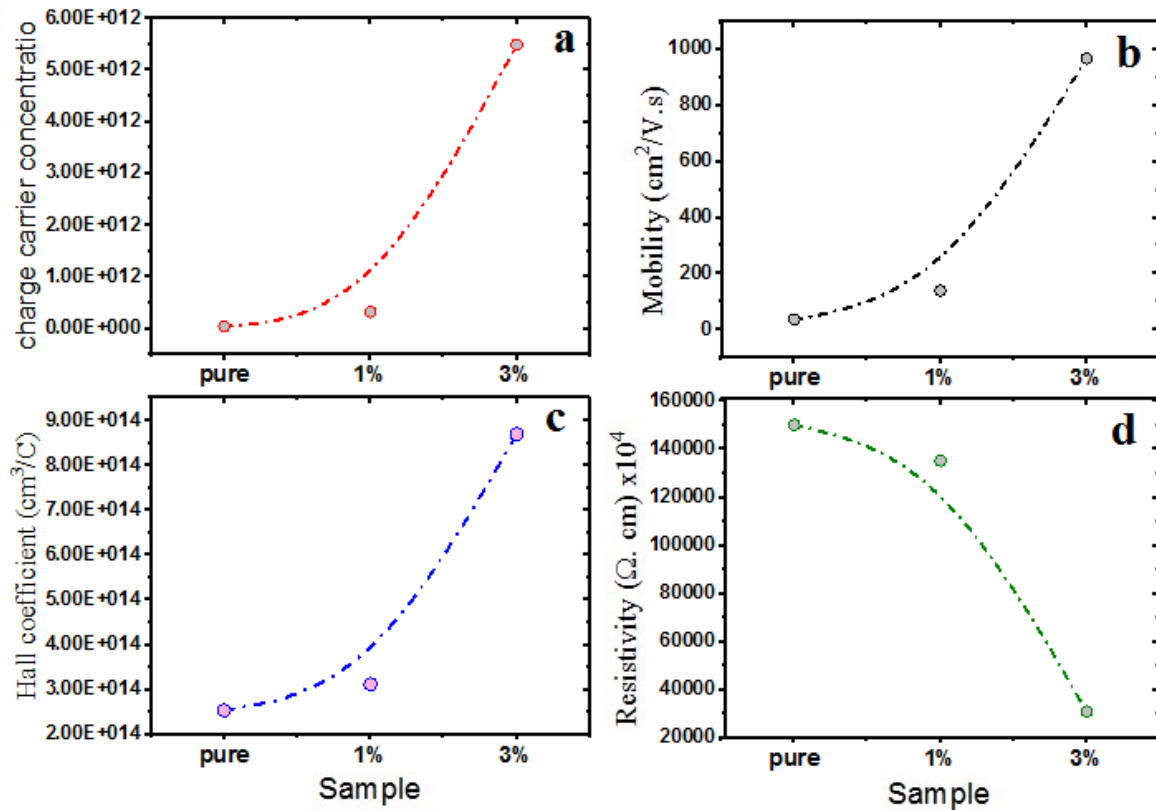


Figure 9. Hall coefficient, resistivity, mobility and charge carriers concentration of the deposited films.

Figure (10) displays the connection between resistance as a function of time of pure Fe₂O₃ and titanium dopant under various hydrogen gas concentrations of (300, 400 and 500 ppm) and at operating temperature of 30°C. Hydrogen molecules (H₂) which is adsorbed in the surface area due to an oxidation process. Some O²⁺ ions shall be removed from the surface and release the bound electrons of atoms O. Such electrons shall drift back to the conduction band [24], causing an increase in the resistance value, and potential barrier under these conditions was improved [25]. It was also noted that the film, which is doped with 3 wt% titanium has the highest resistance to the flow of gas and has the largest ΔR which are directly proportional to the film sensitivity as indicated in the following relation in equation (2) [26].

$$Sensitivity = \frac{\Delta R}{R_g} = \left| \frac{R_g - R_a}{R_g} \right| \times 100 \% \quad (2)$$

The plots of sensitivity as function of Ti content are shown in Figure (11) after being exposed to hydrogen gas. It is found that sensitivity decreases with the increase of doping concentration that is related to the increased of electrical resistance of the film due to the recombination process between the charges that carries the holes with the electrons released from the oxygen. Sensitivity decreases from 61% to 44% for 500 ppm, decreases from 36% to 23% for 400 ppm, and decreases from 30% to 18% for 300 ppm for undoped and Ti-doped Fe₂O₃ respectively. Table (2) represents a comparison between the present works with the previous works

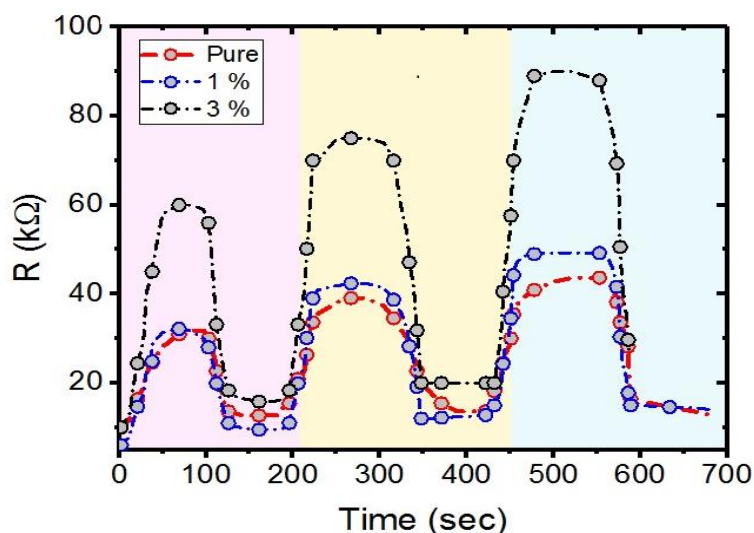


Figure 10. Dynamic Resistance Change of pure and Ti doped Fe_2O_3 Films for Different Concentrations of H_2 gas at an Operating Temperature of $30^\circ C$.

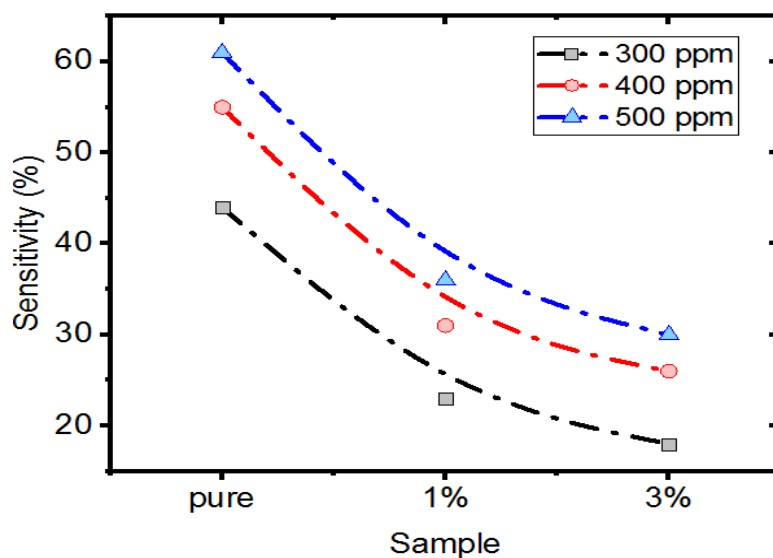


Figure 11. Sensitivity of Fe_2O_3 : Ti films for various concentrations of H_2 gas at $30^\circ C$ operating temperature.

Table 2 Comparison between the present work and previous works

No.	Sample	Target Gas	Concentration (ppm)	Temperature ($^\circ C$)	Response (%)	Ref.
1	α - Fe_2O_3	H_2	1000	500	8.3	[27]
2	α - Fe_2O_3	H_2	5000	80	5-10	[28]
3	Au/ α - Fe_2O_3	H_2	20	40	90	[29]
8	Ti/ α - Fe_2O_3	H_2	500	30	61	This work

4. CONCLUSION

In the current work, nanostructure of undoped and Ti-doped Fe₂O₃ are successfully prepared by the pulsed laser deposition. Crystallite size is very small sizes of (16- 23 nm), which enhanced the electrical and sensing properties of nanostructured Fe₂O₃ films. Best sensitivity was obtained for 3% Ti-doped Fe₂O₃ is 61% at an operating temperature of 150°C for 300 ppm gas concentration. This is the first attempt to utilize this compound as a gas sensor.

ACKNOWLEDGEMENTS

This study is supported by the University of Diyala, College of Science, Diyala, Iraq and AlMustansiriyah University, College of Education, Baghdad, Iraq.

REFERENCES

- [1] Keller, D. A., Ginsburg, A., Barad, H.-N., S.ovich, K., Bouhadana, Y., Rosh-Hodesh, E., Takeuchi, I., Aviv, H., Tischler, Y. R., Anderson, A. Y., Zaban, A. *ACS Comb. Sci.* **17**, 4 (2015) 209–216.
- [2] Limo, M. J., Sola-Rabada, A., Boix, E., Thota, V., Westcott, Z. C., Puddu, V., Perry, C. C., *Chem. Rev.* **118**, 22 (2018) 11118–11193.
- [3] Morales, J. A., *Ciencia en Desarrollo, Enero-Junio de* **8**, 1 (2017) 99-107.
- [4] Kormann, C., Bahnemann, D. W., Hoffmann, M. R., *Journal of Photochemistry and Photobiology A Chemistry* **48**, 1 (1989) 161-169.
- [5] Garcia, D., Picasso, G., Hidalgo, P., Peres, H. E. M., Kou, R. S., Gonçalves, J. M., *Analytical chemistry research* **12** (2017) 74-81.
- [6] Gupta, A. K., Gupta, M., *Biomaterials* **26** (2005)3995–4021.
- [7] Hyeon, T., *Chem. Commun.* **21**, 8 (2003) 927–934.
- [8] Takafuji, M., Ide, S., Ihara, H., Xu, Z., *Chem. Mater.* **16** (2004) 1977–1983.
- [9] Li, Z., Wei, L., Gao, M., Lei, H., *Adv. Mater.* **17** (2005) 1001–1005.
- [10] Dang, Y., and West, A. R., *Journal of the American Ceramic Society* **102**, 1 (2019) 251-259.
- [11] Rahman, G., and Joo O.- S., *international journal of hydrogen energy* **37** 19 (2012) 13989-13997.
- [12] Peerakiatkhajohn, P., Yun, J.-H., Chen, H., Lyu, M., Butburee, T., Wang, L., *Advanced Materials* **28**, 30 (2016) 6405-6410.
- [13] Cheng, Y., Guo, H., Wang, Y., Zhao, Y., Li, Y., Liu, L., Li, H., Duan, H., *Materials Research Bulletin* **105** (2018) 21-27.
- [14] Wu, Z., Li, Z., Li, H., Sun, M., Han, S., Cai, C., Shen, W., Fu, Y. Q., *Appl. Mater. Interfaces* **11**, 13 (2019) 12761-12769.
- [15] Yan, W., Zeng, X., Liu, H., Guo, C., Ling M., Zhou, H., *Chinese Physics B* **28**, 10 (2019) 106801
- [16] Ali, A., Zafar, H., Zia, M., Haq, I. U., Phull, A. R., Ali, J. S., Hussain, A., *Nanotechnol Sci Appl.* **9** (2016) 49–67.
- [17] Huang, M.- C., Chang, W.-S., Lin, J. -C., Chang, Y.-H., Wu, C. -C. , *Journal of Alloys and Compounds* **636** (2015) 176-182.
- [18] Ogale, S. B., Koinkar, V. N., Joshi, S. Godbole, V. P., Date, S. K., Mitra, A., Venkatesan, T., Wu, X. D., *Appl. Phys. Lett.* **53**, 14 (1988)1320-1322.
- [19] Puech, L., Dubarry, C., Ravel, G., Vito, E. d., *Journal of Applied Physics* **107**, 5 (2010) 054908.
- [20] Alagar, M., Theivasanthi T., Raja, A. K., *J. of App. Sci* **12** (2012) 398-401.
- [21] Krauss, I. R., Merlino, A., Vergara, A., Sica, F., *Int J Mol Sci.* **14**, 6 (2013) 11643–11691.
- [22] Khan, H., Swati, I. K., *Ind. Eng. Chem. Res.* **55**, 23 (2016) 6619–6633.
- [23] Luo, Z., Li, C., Liu, S., Wang, T., Gong, J., *Chemical Science* **8**, 1 (2017) 91-100.
- [24] Huberta, T., Boon-Brettb, L., Blackb, G., Banacha, U., *Sensors and Actuators B: Chemical* **157** (2011) 329-352.
- [25] James, A. D., Kristin, D., Terry, A. R., *Sensors and Actuators B: Chemical* **80** (2001) 106 -115.

- [26] Balaguru, R., Bosco, J., Jeyaprakash, B. G., NPTEL–Electrical & Electronics Engineering–Semiconductor Nanodevices **5** (2004) 505–521.
- [27] Long, N. V., Teranishi, T., Thi, Yang, Y., C. M., Cao, Y., Nogami, M., Int. J. Metall Mater Eng. **1**, 119 (2015) 2804-2812.
- [28] Hübert, T. B. -B., Palmisano, L., Frigo, V., Hellstrand, G., Kiesewetter, A. O., May, M., **39** (35) (2014) 20474-20483,
- [29] Kobayashi, T., Haruta, M., San, H., Nakane, M., Sensors and Actuators, **13** (1988) 339–349.